Robust, Stable, and Accurate Boundary Movement for Physical Etching and Deposition Simulation

Ze-Kai Hsiau, Edwin C. Kan, *Member, IEEE*, James P. McVittie, *Senior Member, IEEE*,
and Robert W. Dutton, *Fellow, IEEE*

***Abstract*— The increasing complexity of VLSI device interconnect features and fabrication technologies encountered by semiconductor etching and deposition simulation necessitates improvements in the robustness, numerical stability, and physical accuracy of the boundary movement method. The volume-mesh-based level set method, integrated with the physical models in SPEEDIE, demonstrates accuracy and robustness for simulations on a wide range of etching/deposition processes The surface profile is reconstructed from the well-behaved level set function without rule-based algorithms. Adaptive gridding is used to accelerate the computation. Our algorithm can be easily extended from two-dimensional (2–D) to three-dimensional (3-D), and applied to model microstructures consisting of multiple materials. Efficiency benchmarks show that this boundary movement method is practical in 2-D, and competitive for larger scale or 3-D modeling applications.**

I. INTRODUCTION

DEVELOPMENT of next-generation VLSI with deep submicron technologies has demanded fundamental understanding of the wafer surface reaction kinetics. Modeling of etching and deposition processes has seen increasing use of simulation techniques. To account for the effects from modeling high aspect ratio device features, complex microstructures and a selection of various etching and deposition processes, a robust, numerically stable, and physically accurate boundary movement method is indispensable. For example, etching 10:1 aspect ratio features is becoming commonplace. For high-density plasma (HDP) oxide etching [1], the thickness of the polymer, which develops on the sidewalls, is an order of magnitude smaller than the device feature size. For HDP oxide deposition with sputtering [2], the facet formation is highly dependent on the sputter yield. For silicon etching with sidewall passivation [3], the sidewall slope is determined by the delicate balance of simultaneous etching and deposition. For sputter etch [4], the material removal rates by ion bombardment are angle dependent. The recent interest in using aluminum reflow for high aspect windows and vias as an alternative to CVD via-filling processes [5] also poses a challenge for accurate and robust boundary movement algorithms.

According to [6], the boundary movement problem can be posed in three ways: 1) by representing the boundary as a geometric model, 2) by the method of characteristics, and 3) by solving the partial differential equations for boundary motion. Their spatial discretization methods can be divided into two general categories: 1) the Lagrangian-type method (shorthand denoted as L-type method) and 2) the Eulerian-type method (shorthand denoted as E-type method), as illustrated in Fig. 1. The L-type grid is always aligned with the moving boundary. The E-type grid is stationary, and the geometry can be extracted from certain values stored on the grid points. Many existing etching and deposition simulators such as DEPICT-2 [7] use L-type boundary movement method. The cell method [8], which stores the area ratio in each grid element, is of the E-type, but it is inaccurate in evaluating surface curvature and capturing facet formation accurately. The level set method is also of the E-type. Fig. 2 shows a comparison on robustness, accuracy and stability between the L-type method and the level set method. The first column shows differences for deposition that results in the filling of a contact. A void is formed in the process, and the topology is changed. The L-type method needs rule-based algorithms to resolve the changes in topology, which however may require intricate algorithms and lead to a loss of efficiency and physical accuracy. The level set method can be applied independently of topology, capturing the void without delooping. The second column

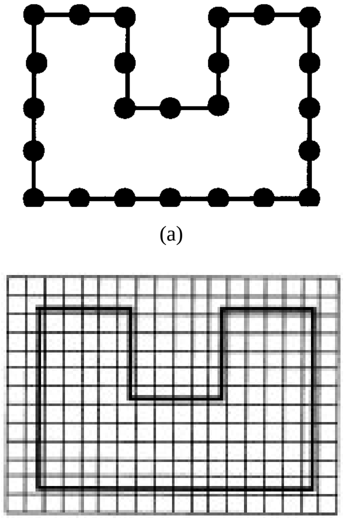

Fig. 1. The two general categories of boundary movement methods. (a) The Lagrangian methods are based on moving grid. (b) The Eulerian methods are based on fixed grid.

Manuscript received August 21, 1996; revised December 23, 1996. The review of this paper was arranged by Editor A. H. Marshak. This work was supported by ARPA under Contract DABT63-93-C-00053 and SRC under Contract 95-IP-404.

The authors are with the Center for Integrated Systems, Stanford University, Stanford, CA 94309 USA.

Publisher Item Identifier S 0018-9383(97)06121-2.

0018–9383/97$10.00

	robustness			accuracy	stability
	void formation	concave corners	convex corners	correct physical interpretation	discretization error
	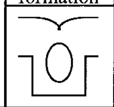	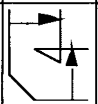	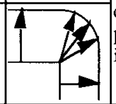		
Lagrangian methods	rule based	rule based delooping	rule based	separate treatments	little control
level-set method	independent of topology	entropy condition (no loops)	entropy condition	no separate treatments	formally analyzed

Fig. 2. The comparison on robustness, physical accuracy, and numerical stability between Lagrangian-type methods and the level set method.

shows deposition over concave corners. With the L-type method, unphysical loops may form, and delooping algorithms are necessary, but this may also lead to loss of efficiency and physical accuracy. No loop will be formed with the level set method. The third column shows how new fronts are created in deposition over convex corners. It is difficult for rule-based algorithms to give a robust and general treatment for all cases. The level set method uses entropy condition to identify the physical boundary nearby geometric singularities. The fourth column addresses the issue of physical accuracy. The computational results of different physical models may use different definitions, which are usually in the form of either the material velocity or the amount of material etched/deposited at each surface grid point. The L-type method needs separate treatment to interpret the output format of the physical models correctly, while the level set method can be applied with a simple adjustment in the velocity definition. The fifth column addresses the issue of numerical stability. There can be little control over the errors due to the rule-based computations in the L-type method, but the error of the level set method can be formally evaluated [9].

All these considerations are even more critical for 3-D simulation [10]–[11]. Acceleration by using larger time steps is difficult with nodal boundaries in which the grid size often limits the time steps. With L-type method, it is also difficult to maintain a detailed accounting of the amount of material etching/deposition for mass conservation, and rule-bases algorithms may offset the precision obtained from accurate physical modeling. The level set method was introduced in [12], and prototyped in [13] and [14] to model idealized etching/deposition problems, where very restrictive assumptions are made on the rate (curvature dependent, uniform or angle dependent) or the source (uniform or unidirectional). Notice that many physical etching/deposition mechanisms are not the superposition of these idealized cases. With these assumptions, the boundary movement can be easily performed on a fixed grid. We have used the level set method as an alternative boundary movement method for the Stanford physical etching/deposition simulator SPEEDIE [15]. The physically-based mechanisms to account for the transport of species in the device feature scale include the steady-state reemission of neutrals [31], the specular reflection of ions [2], the angle dependent sputtering by ions [2], and the redeposition of sputtered materials [2]. The efficient implementation of these mechanisms in SPEEDIE requires the boundary representation of the device geometry, which keeps track of the neighboring information used in searching or traversing the geometry. Thus, dual representations of the geometry, by the fixed and the moving grid, co-exist in our simulations. This hybrid method reflects the most efficient way to our knowledge for integrating the level set boundary movement method with physically-based etching/deposition mechanisms. Section II will show the formulation and implementation of the level set method. Section III will show 2-D calibration results with different fabrication technologies, the potential use for 3-D applications, and discuss the issue of efficiency.

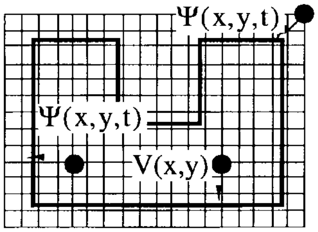

Fig. 3. Definition of the level set function $\Psi(x, y, t)$ and the interpolation of $V(x, y)$.

II. Formulation and Implementation

A. Mathematical Formulation

The boundary can be viewed as a level set of a particular function with one more spatial dimension. As shown in Fig. 3 for the 2-D case, the level set function $\Psi(x, y, t)(\mu\text{m})$ is defined as the signed distance of a point (x, y) to the boundary of the geometry under consideration. $\Psi(x, y, t)$ will be positive if (x, y) is outside the geometry, and will be negative if inside. All points of (x, y) which satisfy

$$0 = \Psi(x, y, t) \tag{1}$$

denote the geometry boundary. The moving boundary is tracked by updating $\Psi(x, y, t)$ over time. Taking the time derivative of (1) and assuming that each boundary point moves along its surface normal result in

$$0 = \frac{\partial \Psi(x, y, t)}{\partial t} + V|\nabla \Psi(x, y, t)| \tag{2}$$

where V has the unit of velocity (μm/s).

This approach represents the sharp corners on the substrate surface as slope singularities of an otherwise smooth surface. The level-set function Ψ is not differentiable at singularities, thereby (2) is ill-defined. A weak formulation of (2) is necessary for general boundary movement problems, in which (2) is valid only on smooth parts of the boundary. Multiple weak solutions could be constructed to satisfy (2) almost everywhere except at singular points [16], [17]. Thus an additional condition is required to identify the unique physical solution among the weak solutions. An entropy condition for slope discontinuities around singular points and an equation for singularity propagation (shocks) can be formulated for topography evolution with the method of characteristics [6], [18]. The entropy condition, which is in this case equivalent

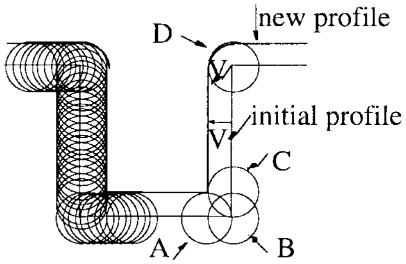

Fig. 4. Illustration of the entropy condition with Huygens' Principle.

to envelope construction by Huygens' Principle [19], is physically reasonable and is illustrated in Fig. 4 for the case of uniform deposition over a rectangular trench. All circles have centers on the original boundary and have a radius equal to V. The new profile nearby the top right corner is delineated by circle D. The new profile nearby the bottom right corner is delineated by circles A and C, and all circles between circle A and C (such as circle B) do not contribute to the new profile.

In some APCVD environments, the flow-like behaviors [20] of the deposition profile suggests the introduction of substrate curvature dependent mechanism in surface deposition kinetics. However, in most of the low-pressure etching/deposition environments we consider, this curvature dependency is not observed. To provide a consistent framework for topography evolution, a formulation based on surface reaction site competition is derived below. For the purpose of illustration, a unit process step of deposition is considered. A generic two-step deposition mechanism can be expressed as precursor adsorption followed by surface reaction

$$\text{Adsorption:} \qquad A_{(g)} + * \Rightarrow A^*_{(s)} \tag{3}$$

$$\text{Surface Reaction:} \quad A^*_{(s)} \Rightarrow S_{(s)} + R_{(g)} + * \tag{4}$$

where A is the deposition precursor, $*$ is the surface reaction site, S is the solid-phase deposition product, and R is the gas-phase reaction by-product. We will let k_{ad}, k_{de}, and k_{sr} (molecule/μm^{2}s) denote the adsorption, desorption, and surface reaction rate constant, respectively. Similar to [21], let the adsorption probability of the precursor be s_* (unitless) on available sites (zero on occupied sites), the surface coverage of available sites be θ_* (unitless), the surface coverage of occupied sites be θ_{A^*} (unitless), and J_A (molecule/μm^{2}s) be the precursor impingement flux. Then the adsorption rate $R_{\text{ad}} = s_* J_A \theta_*$ (molecule/μm^{2}s) will be equal to the depletion rate of A^* in dynamic balance. If the normalized conservation of surface sites can be expressed as $\theta_* + \theta_{A^*} = f(K)$ (unitless), where K (1/μm) is the local substrate curvature defined in 2-D as (subscripts denote partial derivatives)

$$K = \frac{\Psi_{yy}\Psi_x^2 - 2\Psi_x\Psi_y\Psi_{xy} + \Psi_{xx}\Psi_y^2}{\left(\Psi_x^2 + \Psi_y^2\right)^{3/2}} \ (1/\mu\text{m}) \tag{5}$$

then the resulting deposition rate is

$$\begin{aligned} R_D &= \theta_{A^*} k_{\text{sr}} f(K) \\ &= \frac{s_* k_{\text{sr}} J_A}{s_* J_A + k_{\text{de}} + k_{\text{sr}}} f(K) \ (\text{molecule}/\mu\text{m}^2\text{s}). \end{aligned} \tag{6}$$

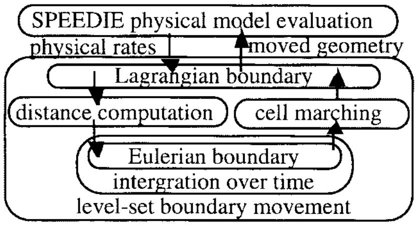

Fig. 5. The flow chart of one cycle of SPEEDIE simulation.

If the surface saturation factor (unitless) is defined as

$$S_a = \frac{s_* J_{A0}}{k_{\text{de}} + k_{\text{sr}}} \ (\text{unitless}) \tag{7}$$

with J_{A0} being the total impingement on entirely planar surfaces, S_a governs the relative ratio of θ_* and θ_{A^*}. The net deposition rate R_D now becomes

$$R_D = \frac{S_a \hat{J}_A}{1 + S_a \hat{J}_A} k_{\text{sr}} f(K) \ (\text{molecule}/\mu\text{m}^2\text{s}) \tag{8}$$

where $\hat{J}_A = J_A/J_{A0}$ (unitless) accounts for all first-order geometrical effects. The limiting cases of $S_a \rightarrow 0$ (adsorption-limited) for a first-order reaction and $S_a \rightarrow \infty$ (surface-reaction-limited) for a zero-order reaction is well illustrated in [21]. Moreover, if λ (μm) is defined as a phenomenological length to express the thickness of a region above the surface profile, and if the reaction site density is assumed to be constant within this region, the deposition rate modulation factor $f(K)$ can be expressed as

$$f(K) = \frac{2}{1 + \sqrt{1 + 2K\lambda}} \ (\text{unitless}) \tag{9}$$

for 2-D cases as in the infinite-trench approximation. The curvature term compensates and corrects for the local reaction sites loss or growth by geometrical effects of nonplanar surface according to reaction site conservation. A more detailed derivation of (2) and (9), and extension to 3-D can be found in [22]. With (8) and (9), V can be evaluated as

$$V = \frac{R_D}{\rho} \ (\mu\text{m/s}) \tag{10}$$

where ρ (molecule/μm^3) is the density and R_D is computed according to the specific physical model at each point on the boundary. Note that in most of the low-pressure environment, the topography evolution is rate limited by gas phase factors rather than by the surface reaction site density. Hence, $\lambda \approx 0$ can be assumed, the rate modulation factor $f(K)$ reduces asymptotically to 1, and the curvature dependency disappears. This can interpret correctly experimental results from many low-pressure etching/deposition processes, such as the behavior of deposition profile due to surface roughness [23].

A complex geometry with multiple material regions can also be treated with the level set method [24]. Each individual material region is represented by a separate level-set function. $V(x, y)$ at the exposed surface of each region is computed according to the specific physical model with its respective material properties. Equation (2) is then integrated

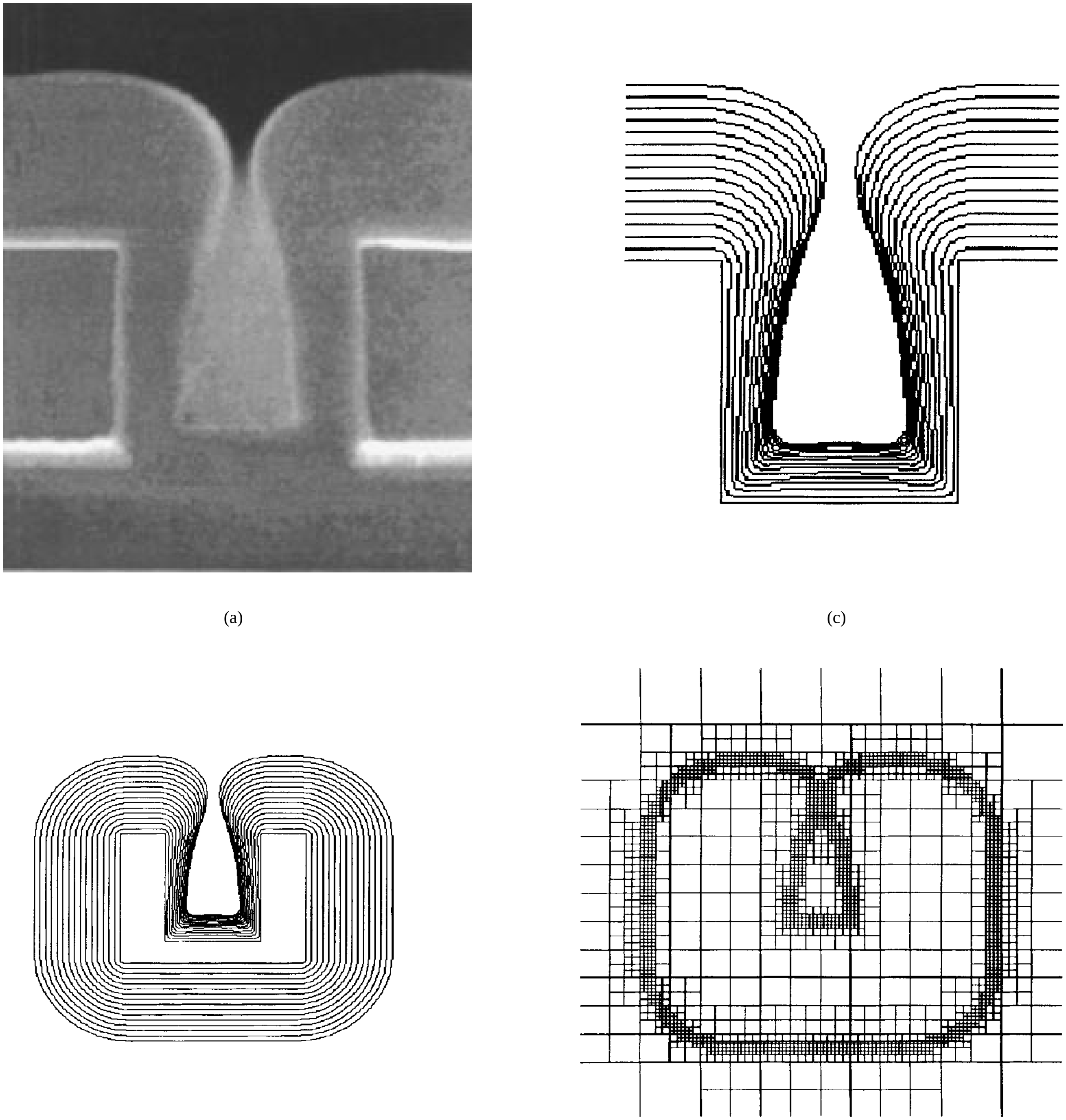

(a) (c)

(b) (d)

Fig. 6. LPCVD of SiO_2 from silane in a trench. (a) The SEM [30]. Process conditions: 380 °C, 250 mTorr, $S_c = 0.35$, $SiH_4/N_2/O_2/PH_3$. (b) The simulated profile evolution. (c) The close-up of the region of interest in (b). (d) The adaptive quad-tree mesh corresponding to the final profile.

for each region. Since each region is moved independently, a consistency criterion [24]

$$\Psi_i = \Psi_i - \min_{j \neq i} \Psi_j \tag{11}$$

can be imposed to maintain consistent common interface between any pair of adjacent regions.

B. Discretization and Solution Schemes

For the spatial discretization of (2), the central difference scheme is used. Since $\Psi(x, y, t)$ is important only in the vicinity of the boundary, and the velocity $V(x, y)$ can only be meaningfully computed by physical modeling on the boundary, adaptive gridding methodology can be applied without loss of generality. This also saves the computation at the points which hold little information about the boundary. The narrow-band method [25] incurs significant complexity in maintaining an update matrix to register the location of a thin tube around the boundary, and in reinitializing the grid to keep the moving boundary within the tube. The level set method on adaptive quad/oct-tree mesh [26] is a more straightforward alternative,

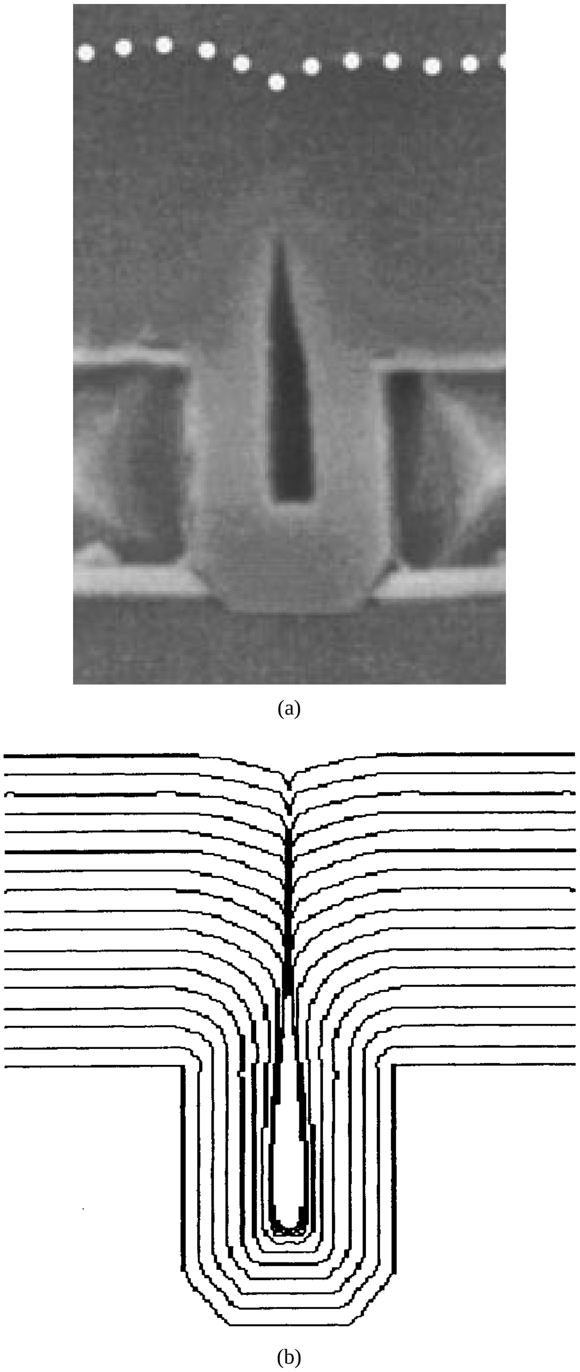

(a)

(b)

Fig. 7. PECVD of SiO_2 from TEOS in a trench. (a) The SEM [32]. Process conditions: 375 °C, 2.1 Torr, $S_c = 0.07$, incoming ion impact-angle distribution: $\cos^{10}(\theta)$, ratio of neutral-to-ion component $= 2$, TEOS flow rate $= 1.8$ sccm, O_2 flow rate $= 6.5$ slm. (b) The simulated profile evolution.

and is more compatible with the adaptive gridding schemes in process simulation environment [27]. In our implementation, adaptive quad-tree mesh, with grid density adapted to $\Psi(x, y, t)$, is used for the spatial discretization of boundary movement [28]. The stopping criteria for adaptivity is

$$\text{cell area} > \bar{\Psi}^2 \text{ or maximum grid density has been achieved} \tag{12}$$

where $\bar{\Psi}$ is the average distance of $\Psi(x, y, t)$ over the quad/oct-tree mesh element.

For the temporal discretization of (2), the forward Euler scheme is used. Typically the time scale for surface reactions Δt_R is much smaller than the other time scales considered below. Let Δt_T denote the characteristic time scale for gas phase transport across feature size. It is assumed in our simulation that the gas phase material balance resulting from surface reemission has been established, and the incident chemical fluxes on the substrate surface have reached the equilibrium values. Thus, the time resolution is limited by Δt_T and Δt_R. Lastly, let Δt_v denote the time scale that the surface profile will not advance too much to introduce large discretization error in visibility calculations. The time step Δt must be less than Δt_v. It is presented in [29] that $\Delta t_v \gg \Delta t_T$ in most fabrication environments. In our implementation of solution schemes on adaptive grid, Δt_v is chosen to be the value such that $\Delta t_v \bullet V \approx d$, where V denotes the maximum surface velocity, and d denotes the minimum grid length. Therefore the adaptation level, or equivalently the minimum grid length d, controls both the spatial and temporal discretization error. The constraint $\Delta t < \Delta t_v$ can be restated as: the boundary should not move more than d within a time step.

In summary, the solution scheme can be written as

$$\Psi(x, y, t + \Delta t) = \Psi(x, y, t) - \Delta t V(x, y) |\nabla \Psi|. \tag{13}$$

Note that $V(x, y)$ in (13) is computed only on the boundary, but a value is required at each grid point in order to support the integration of (13). Since only the values on the grid points nearby the boundary are important, the $V(x, y)$ at each grid point is chosen to be that of its closest point on the boundary, as shown in Fig. 3. Fig. 5 illustrates the implementation of the level-set boundary movement in SPEEDIE.

III. CALIBRATION WITH TECHNOLOGY EXAMPLES

A. Low-Pressure Chemical Vapor Deposition (LPCVD) [30]

Fig. 6(a) shows the scanning electron microscopy (SEM) of the LPCVD SiO_2 deposition profile in a rectangular trench with aspect ratio 1.25, from $SiH_4/N_2/O_2/PH_3$ mixture at 380 °C and 250 mTorr. Fig. 6(b) shows the simulated temporal evolution of the deposition profiles on a cross section of the trench. The deposition model with a single reactive species of intermediate rate limiting neutral precursor is used. The direct neutral flux is computed with the assumption that the gas phase has a Maxwellian velocity distribution, resulting from thermodynamic equilibrium. The reemission mechanism of this chemical component is accounted for by a medium reactive sticking coefficient (Sc) of 0.35 [31]. Instead of tracking only the top surface profiles, as most Lagrangian boundary movement methods with surface-mesh do, the volume-mesh, level set method traces a closed curve. Fig. 6(c) shows a close-up rendering of the region of interest in Fig. 6(b). Fig. 6(d) shows the adaptive quad-tree mesh corresponding to the final profile. Notice that the adaptive mesh has maximum grid density within two grid lengths on either side of the boundary, which limits the time steps. The adaptive quad-tree mesh will incur no loss of generality and accuracy in comparison to the

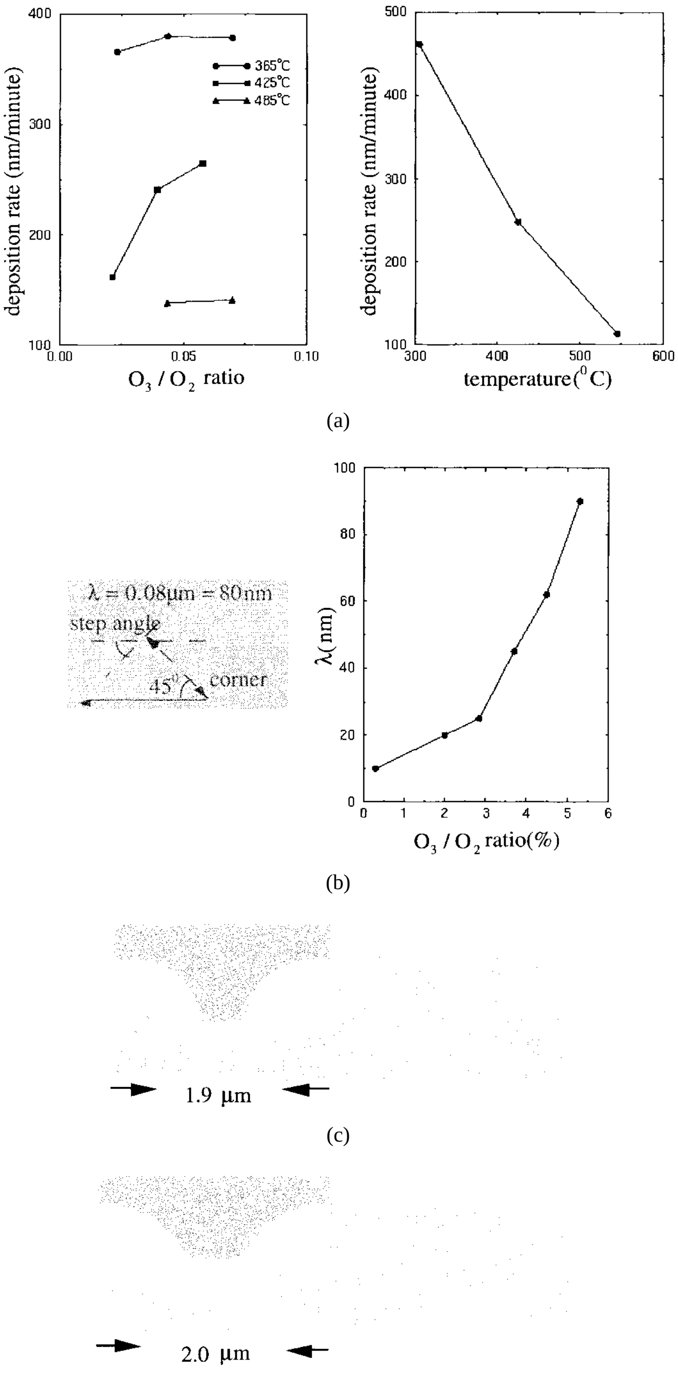

Fig. 8. APCVD of SiO_2 from TEOS/O_3 in a trench [20]. (a) Extraction of deposition rate in APCVD. (b) Extraction of λ in APCVD. The relation between O_3/O_2 ratio and step angle is found in [35]. The relation between λ and step angle is found from simulation. Correlation of these two relations results in the curve shown on the right. (c) The SEM on the left shows the conformal deposition profile by APCVD with low ozone concentration (2.5 g/m^3, 0.13% in the O_3/O_2 stream, 0.05% in the reaction chamber). On the right, the simulated profile evolution with $\lambda = 0.00$ μm is shown. (d) The SEM on the left shows the deposition profile with flow-like behavior by APCVD with high ozone concentration (135 g/m^3, 6.9% in the O_3/O_2 stream, 2.4% in the reaction chamber) is shown. On the right, the simulated profile evolution with $\lambda = 0.02$ μm is shown.

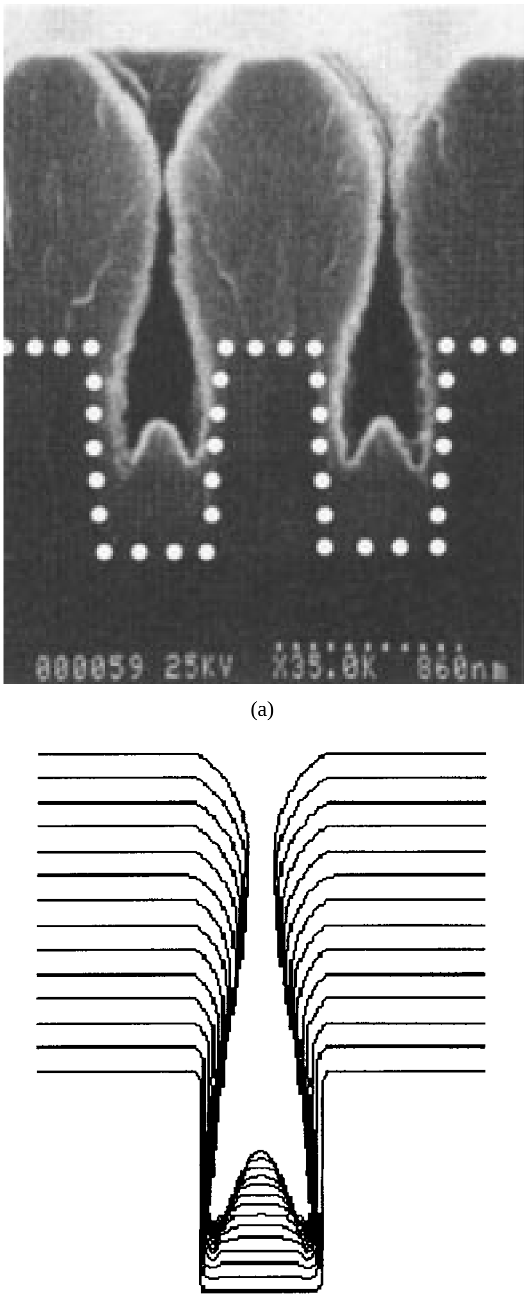

Fig. 9. Ionized magnetron physical vapor deposition of aluminum in a trench. (a) The SEM [36]. (b) The simulated profile evolution. Simulation conditions: temperature below 100 °C, 35 mTorr, $S_c = 1.0$, unidirectional ion distribution, neutral-to-ion flux ratio $= 7{:}3$, sputter yield $= 0.0$.

full tensor product mesh. No points are added at top surface corners, and no unphysical loops are formed at bottom surface corners. The accurate simulation of bread-loafing at the top corners, which is important in the prediction of void formation, is observed.

B. Plasma Enhanced Chemical Vapor Deposition (PECVD) [32]

Fig. 7(a) shows the SEM picture of the PECVD SiO_2 film deposited in a rectangular gap with AR 1.25 between aluminum lines on both sides. The operating point of the experiment is at 375 °C and 2.1 Torr. The gas source is O_2/TEOS (tetraethylorthosilicate) mixture. Fig. 7(b) shows the simulated temporal evolution of the deposition profiles. The

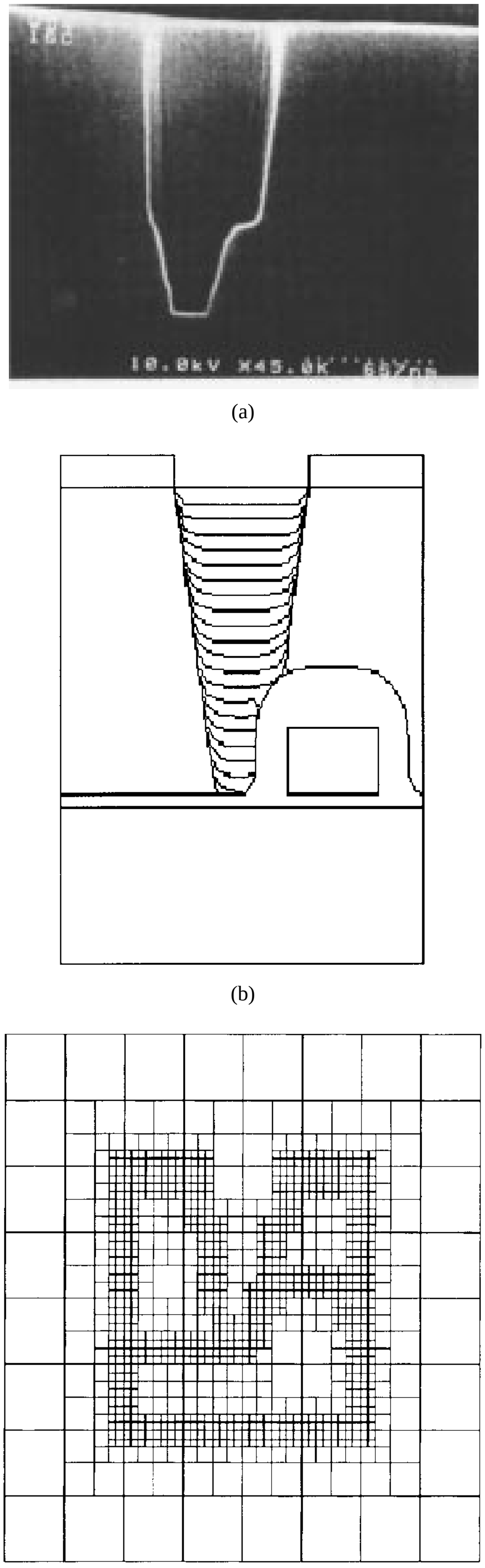

(a)

(b)

(c)

Fig. 10. Self-alignment contact. (a) The SEM, courtesy of J. Nulty, Cypress Semiconductors. (b) The simulated profile evolution. The two mask pieces, oxide, nitride, and substrate are each represented by a separate region and its respective level set function. (c) The adaptive quad-tree mesh corresponding to the final profile.

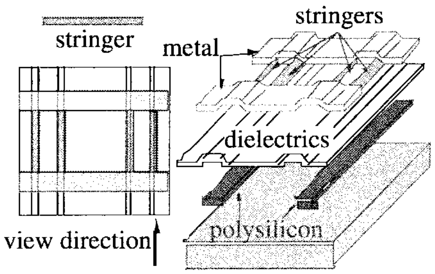

Fig. 11. Schematics of the stringer formation. The left shows the top view. The right shows the blow-up of the involved layers.

deposition model is based on a combination of dual profile-controlling mechanisms: one for LPCVD induced by one neutral precursor with a low reemission sticking coefficient 0.07, and one for ion-induced deposition activated by ion bombardment. Since the ion mean free path of about 100 μm is small in comparison to the plasma sheath thickness of 2 mm, the ion impact angle distribution is determined by sheath acceleration and collisions over the last few mean free paths above the surface, which is best fitted by an analytical cosine distribution with exponent 10. The neutrals, sufficiently randomized through collisions in the gas phase, are assumed to have isotropic angular distribution. The ratio of the LPCVD component to the ion-induced deposition component at the top surface is 2. The void is captured and separated from the top surface profile without special rules. Since the ions activate neutral precursors on the surface, the direct ion impingement is the dominant factor in ion-induced deposition. If the incoming ion distribution is fairly anisotropic, the ion-induced deposition will be a sensitive function of local visibility. Due to discretization errors, the jaggedness in the simulated surface profile may occur. The unphysical shadowing effect by adjacent surface irregularities accumulates over the progression of simulation and may lead to numerical instability. The level set method can be easily controlled to generate smooth surface profiles, without compromising its ability to capture and preserve the sharp corners.

C. Atmospheric Pressure Chemical Vapor Deposition (APCVD) [20]

It has been demonstrated that the ozone concentration can affect the degree of the flow-like behavior of silicon dioxide films deposited from tetraethylorthosilicate (TEOS) and ozone (O_3) [33]. The curvature dependency model in II.A can account for this flow-like behavior. $\hat{J}_A$ in (8) can be computed in the SPEEDIE physical model. When MFP $\ll$ feature size $\ll$ injector/substrate spacing, $\hat{J}_A \approx 1$ [34]. S_a in (8) can be extracted from the experimental deposition rate on planar surfaces [35], as shown in Fig. 8(a), if J_{A0} in (7) or the rate constants can be derived from other measurement/equipment-modeling or first-principle calculations [21]. λ can be extracted from the experimental curves of the step angles (more error) or the corner thickness vs. the O_3/O_2 ratio [33], as shown in Fig. 8(b). On the left of Fig. 8(c), the SEM of the conformal deposition profile by APCVD with low ozone concentration (2.5 g/m^3, 0.13% in the O_3/O_2 stream, 0.05% in the reaction chamber) is shown. On the right of Fig. 8(c), the simulated profile evolution with $\lambda = 0$ is shown. On the left of Fig. 8(d),

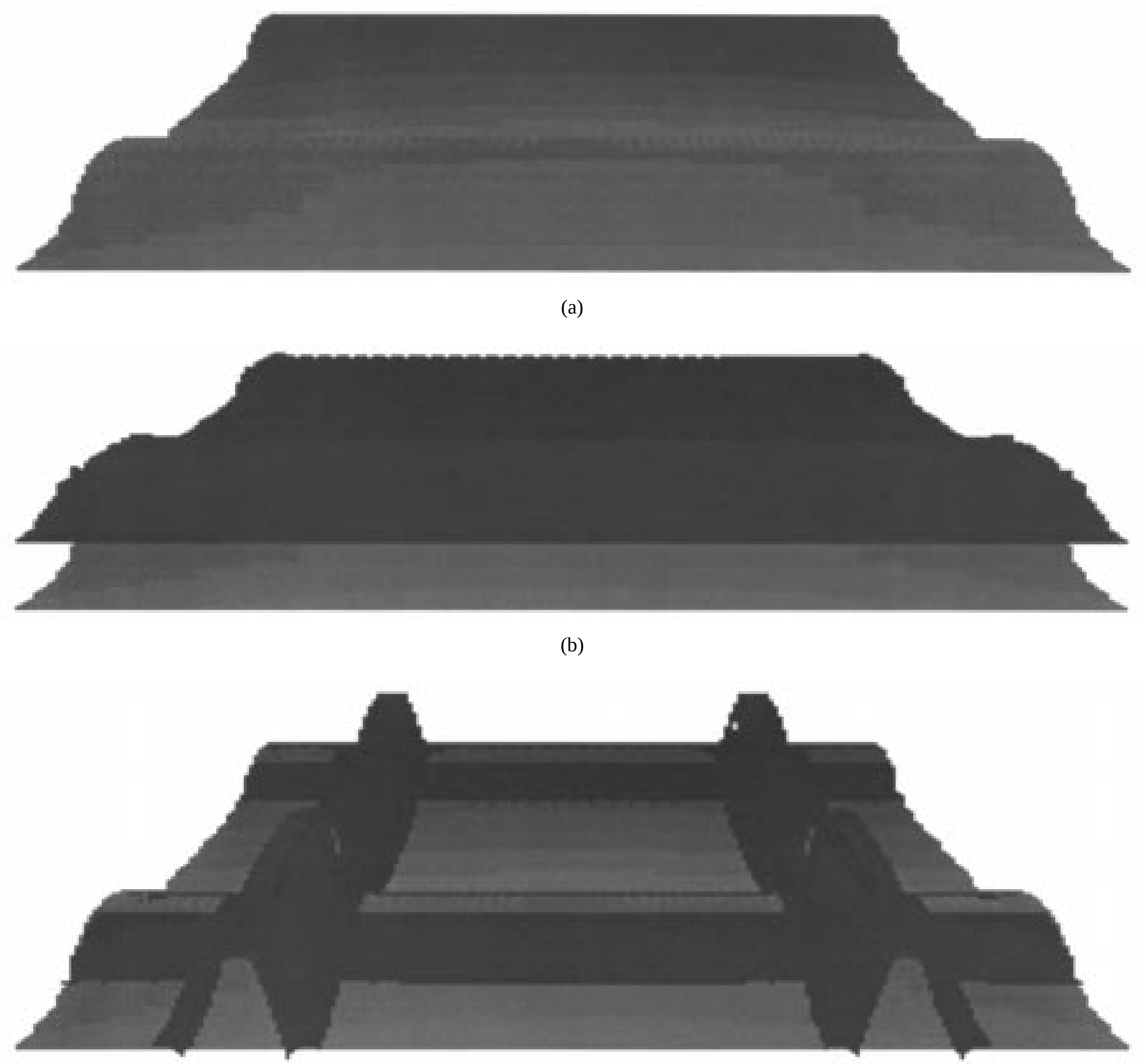
(a)

(b)

(c)

Fig. 12. 3-D perspective views of the stringer formation. (a) The dielectrics (the lighter gray) before blanket deposition of Al. (b) After blanket deposition of Al. Al (the darker gray) is on top of the dielectrics (the lighter gray). (c) After etchback of Al to pattern the interconnect lines.

the deposition profile with flow-like behavior by APCVD with high ozone concentration (135 g/m^3, 6.9% in the O_3/O_2 stream, 2.4% in the reaction chamber) is shown. On the right of Fig. 8(d), the simulated profile evolution with $\lambda = 0.02$ μm is shown. From these comparisons, it can be seen that the 0th-(planar growth rate), 1st-(microstructure shape), and second-order (curvature) can be well modeled.

D. Ionized Magnetron Sputter Metal Deposition [36]

Fig. 9(a) shows the SEM picture of the blanket deposition of aluminum thin film in argon discharge on a rectangular SiO_2 trench with an AR of 2. The wafer temperature is maintained below 100 °C by substrate cooling. Fig. 9(b) shows the simulated temporal deposition profile evolution. The simulation is conducted under the following conditions:

1) The argon discharge pressure is maintained at 35 mTorr for high ionization with mean free path of about 2.5 mm. The motion of sputtered atoms from the magnetron target is sufficiently randomized through collisions in the gas phase with a cutoff angle close to 90°, so an isotropic angular distribution can be assumed. The sticking coefficient of this neutral species is assumed to be 1.
2) An appropriate low dc bias voltage ($\leq$20 V) is applied, so the sputter yield and redeposition is negligible. However, the ion acceleration through the 0.1-mm thick sheath adjacent to the sample wafer is still practically collisionless, so the ion impact-angle distribution can be assumed to be unidirectional.
3) The ratio of the magnetron discharge power to the radio-frequency induction coil power is 3:1, with which the ratio of the neutral component to the ion component at the top flat surface can be controlled to be 7:3.

Two important measures of the quality of deposition are the top coverage (the film thickness on the top flat surface) and

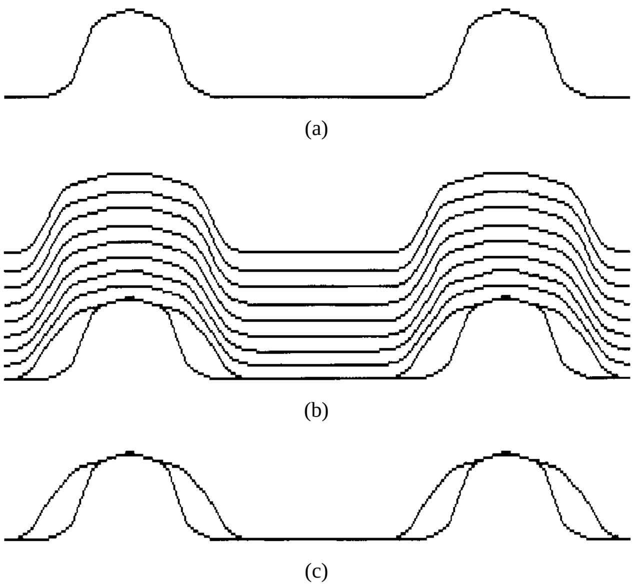

Fig. 13. 2-D profile evolution on the cut plane, as indicated in Fig. 12(a) of the stringer formation. (a) Before blanket deposition of Al. (b) After blanket deposition of Al. (c) After etchback of Al to pattern the interconnect lines.

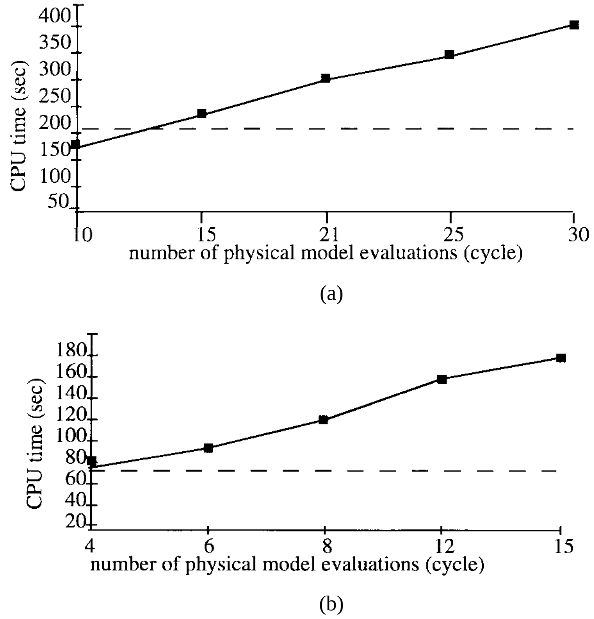

Fig. 14. Efficiency benchmark. (a) shows the efficiency benchmark with LPCVD simulation in a trench with 85 surface grids. The dashed horizontal line denotes the execution time of SPEEDIE using the L-type boundary movement method with 150 cycles of physical model evaluation and boundary movement. The solid line denotes the execution time of SPEEDIE with the level set boundary movement method against the number of simulation cycles. (b) shows the corresponding chart for PVD. This simulation uses 82 surface grids and 120 cycles.

the bottom coverage (the film thickness at the center of the bottom). A good prediction of these two metrics is observed with the simulated final profile. The deposition at the bottom corners is blocked by the effect of shadowing incoming ions by the top corners. These sharp corners are captured by the level set method without extra grid density.

E. Self-Alignment Contact

Fig. 10(a) shows the SEM picture of the formation of self-alignment contact. Fig. 10(b) shows the simulated profile evolution. The oxide is etched down to form a contact. If the mask is not aligned as seen in the figure, the underlying poly-Si is protected from etching by the nitride layer. The etch rates are reduced by the inhibitor, which is due to the formation of polymer on the sidewalls. In this process, simultaneous etching and deposition compete at each surface site on the sidewalls until an equilibrium with zero net etch rates is established. Less etching and more polymer formation will occur on steeper sidewalls. The balance of sidewall etching and polymer formation determines the sidewall slopes. This example also serves to show an application of the level set method on more complex geometry. When the etching profile reaches the nitride, the exposed top surface profile consists of the two masks, the sidewalls, and the top surface of the nitride. The two mask pieces, the oxide, the nitride, and the substrate are each represented by separate level set functions. In Fig. 10(c), the grid adaptation criteria in (12) now uses the arithmetic average of all level set functions. Each boundary is moved independently, and then the consistency criteria in (11) is applied to all moved boundaries to maintain a common interface.

F. Stringer Formation [37]

In patterning interconnect metal lines on nonplanar surfaces, metal stringers may appear and thereby short adjacent lines. Fig. 11 illustrate the schematics of the stringer formation process. Interlayer dielectric is deposited on top of the poly-Si lines with near-vertical sidewalls. Aluminum is then blanket deposited on this nonplanar surface, followed by the etch step to pattern the lines. After the etch profile of aluminum on the top flat surface has just cleared, stringers may be present against the near-vertical step over the underlying topography. If not removed, they would result in conducting paths between metal lines. These stringers are usually removed by long over-etch with 100–200% of the main etch time. With the reduction in metal line-width and film thickness, precise etch profile control with minimal critical dimension loss is becoming more critical. The perspective view of our 3-D simulation with the level set boundary movement method is shown before the blanket deposition in Fig. 12(a), after the blanket deposition in Fig. 12(b), and after the main etch step in Fig. 12(c). Their corresponding 2-D views on the cut plane are shown in Fig. 13(a)–(c). Stringers analysis exemplifies the need to resolve microscopic scale feature in 3-D.

IV. EFFICIENCY

The level set boundary movement method is, in general, computationally more expensive than the rule-based L-type methods, but larger time steps may be taken as a result of more controllable discretization errors. Therefore, for a fixed simulation time, the number of simulation cycles for the level set boundary movement method can be lower than the L-type methods, and hence the time spent on physical modeling computation can be reduced. In situations where physical model evaluation is more significant, such as in complex geometry and for 3-D models, the time saved on physical model computation can offset the overhead for the level set boundary movement. Fig. 14(a) shows the efficiency benchmark with LPCVD simulation in a trench with 85 surface grids. The dashed horizontal line denotes the execution time of SPEEDIE using L-type boundary movement method with 150 cycles of physical model evaluation and boundary movement. The solid line denotes the execution time of SPEEDIE with the level set boundary movement method against the number of physical model evaluation cycles. The boundary evolution (2) is integrated 150 times, which are equally distributed in all simulation cycles. The rightmost data points in Fig. 14(a) indicates a simulation with 30 cycles, in each of which (2) is integrated five times. The accuracy of this simulation is comparable to that of the simulation with the L-type boundary movement method (indicated by the dashed line). Fig. 14(b) shows the corresponding chart for PVD simulation in a trench with 82 surface grids and 120 simulation cycles. In this case, the physical model evaluation is faster due to the assumption in our simulation that the sticking coefficient is 1. For modeling HDP deposition, the SPEEDIE simulation using the level set boundary movement method with 40 cycles and 1038 CPU seconds achieves comparable accuracy as the SPEEDIE simulation using the L-type boundary movement method with 150 cycles and 916 CPU seconds. The performance penalty for the level set boundary movement method drops with the more complex physical models, such as the HDP deposition model.

V. CONCLUSION

Through examples of various etching and deposition techniques, it is demonstrated that the level set boundary movement method can be robust, stable and accurate. This method is computationally more expensive, yet in general allows for larger time steps than the L-type methods and may achieve comparable accuracy. We observed that this method is practical in terms of efficiency, and competitive in large-scale computation such as in complex geometry and 3-D.

ACKNOWLEDGMENT

The authors wish to thank Prof. Neureuther, the University of Berkeley, for allowing access to SAMPLE-3D to evaluate 3-D string methods, and J. Nulty, Cypress Semiconductor, for providing the SEM picture of the self-alignment contact experiment.

REFERENCES

[1] J. S. Han, J. P. McVittie, and J. Zheng, "Profile modeling of high-density plasma oxide etching," *J. Vac. Sci. Technol. B*, vol. 13, no. 4, July/Aug. 1995.

[2] C. Y. Chang, J. P. McVittie, J. Li, K. C. Saraswat, S. E. Lassig, and J. Dong, "Profile simulation of plasma enhanced and ECR oxide deposition with sputtering," in *IEDM Tech. Dig.*,1993, p. 853.

[3] J. Zheng and J. P. McVittie, "Modeling of side wall passivation and ion saturation effects on etching profiles," *NUPAD V Tech. Dig.*, p. 37, 1994.

[4] C. Y. Chang, J. P. McVittie, K. C. Saraswat, and K. K. Lin, "Backscattered deposition in Ar sputter etch of silicon dioxide," *Appl. Phys. Lett.*, vol. 63, no. 16, pp. 2294–2296, Oct. 1993.

[5] F. H. Baumann and G. H. Gilmer, "3-D modeling of sputter and reflow processes for interconnect metals," in *IEDM Tech. Dig.*, 1995, p. 89.

[6] S. Hamaguchi, M. Dalvie, R. T. Farouki, and S. Sethuraman, "A Shock-tracking algorithm for surface evolution under reactive-ion etching," *J. Appl. Phys.*, vol. 74, no. 8, pp. 5172–5184, Oct. 1993.

[7] DEPICT-2, *Technology Modeling Associates*, 1990.

[8] S. Yamaguchi, "Three-dimensional simulation technology," *Semiconductor World*, pp. 149–153, Jan. 1990, (in Japanese).

[9] D. J. Benson, "Computational methods in Lagrangian and Eulerian hydrocodes," *Comp. Methods Appl. Mech. Eng.*, vol. 99, pp. 235–394, 1992.

[10] A. R. Neureuther *et al.*, "3-D Topography simulation using surface representation and central utilities," *Three-Dimensional Process Simulation*, J. Lorenz, Ed. New York: Springer-Verlag, 1995, p. 57.

[11] E. W. Scheckler, "Algorithm for three-dimensional simulation of etching and deposition processes in integrated circuit fabrication," Tech. Memo. *UCB/ERL M91/99*, Electronics Research Laboratory, Univ. California, Berkeley, Nov. 1991.

[12] S. Osher and J. A. Sethian, "Fronts propagating with curvature-dependent speed: Algorithms based on Hamilton-Jacobi formulations," *J. Comp. Phys.*, vol. 79, pp. 12–49, 1988.

[13] D. Adalsteinsson and J. A. Sethian, "A level set approach to a unified model for etching, deposition, and lithography I: Algorithms and two-dimensional simulations," *J. Comp. Phys.*, vol. 120, no. 1, pp. 128–144, 1995.

[14] ——, "A level set approach to a unified model for etching, deposition, and lithography II: Three-dimensional simulations [Integrated circuits]," *J. Comp. Phys.*, vol. 122, no. 2, pp. 348–366, 1995.

[15] J. P. McVittie, D. S. Bang, J. S. Han, K. Hsiau, J. Li, J. Zheng, and K. C. Saraswat, *SPEEDIE V3.0 User's Manual*, Stanford Univ., Stanford, CA, Aug. 1995.

[16] R. E. Jewett, P. I. Hagouel, A. R. Neureuther, and T. van Duzer, "Line-profile resist development simulation techniques," *Polym. Eng. Sci.*, vol. 17, p. 381, 1977.

[17] W. Fichtner, "Process simulation," *VLSI Technology*, 2nd ed. S. M. Sze, Ed. New York: McGraw-Hill, 1988.

[18] J. C. Arnold, H. H. Sawin, M. Dalvie, and S. Hamaguchi, "Simulation of surface topography evolution during plasma etching by the method of characteristics," *J. Vac. Sci. Technol. A*, vol. 12, no. 3, pp. 620–635, May/June 1994.

[19] J. A. Sethian, "Curvature and the evolution of fronts," *Commun. Math. Phys.*, vol. 101, pp. 487–499, 1985.

[20] J. Li, "Topography simulation of intermetal dielectric deposition and interconnection metal deposition processes," Ph.D. thesis, Dept. Mech. Eng., Stanford Univ., Stanford, CA, 1996.

[21] J. J. Hsieh, "Influence of surface-activated reaction kinetics on low-pressure chemical vapor deposition conformality over micro features," *J. Vac. Sci. Technol. A*, vol. 11, no. 1, pp. 78–86, Jan./Feb. 1993.

[22] Z. K. Hsiau "Boundary movement problem in semiconductor etching and deposition simulation," Ph.D. thesis, Dept. Comp. Sci., Stanford Univ., Stanford, CA, 1997.

[23] V. K. Singh and E. S. G. Shaqfeh, "Effect of surface reemission on the surface roughness of film growth in low-pressure chemical vapor deposition," *J. Vac. Sci. Technol. A*, vol. 11, no. 3, pp. 557–568, May/June 1993.

[24] B. Merriman, J. K. Bence, and S. J. Osher, "Motion of multiple junctions: A level set approach," *J. Comp. Phys.*, vol. 112, pp. 334–363, 1994.

[25] D. Adalsteinsson and J. A. Sethian, "A fast level set method for propagating interfaces," *J. Comp. Phys.*, vol. 118, no. 2, pp. 269–277, 1995.

[26] B. Milne, "Adaptive level set methods interfaces," Ph.D. thesis, Dept. Math., Univ. California, Berkeley, 1995.

[27] Z. H. Sahul, K. C. Wang, Z. K. Hsiau, E. W. McKenna, and R. W. Dutton, "Heterogeneous process simulation tool integration," *IEEE Trans. Semiconduct.Manufact.*, vol. 9, pp. 35–48, Feb. 1996.

[28] Z. K. Hsiau, E. C. Kan, J. P. McVittie, and R. W. Dutton, "Physical etching/deposition simulation with collision-free boundary movement," in *IEDM Tech. Dig.*, 1995, p. 101.

[29] H. C. Wulu, K. C. Saraswat, and J. P. McVittie, "Simulation of mass transport for deposition in via holes and trenches," *J. Electrochem. Soc.*, vol. 138, no. 6, pp. 1831–1840, June 1991.

[30] M. M. IslamRaja and M. A. Cappelli, "A three-dimensional model for low-pressure chemical-vapor-deposition step coverage in trenches and circular vias," *J. Appl. Phys.*, vol. 70, no. 11, pp. 7137–7140, Dec. 1991.

[31] J. P. McVittie, J. C. Rey, L. Y. Cheng, M. M. IslamRaja, and K. C. Saraswat, "LPCVD profile simulation using a reemission model," in *IEDM Tech. Dig.*, 1990, p. 917.

[32] J. Li, J. P. McVittie, J. Ferziger, and K. Saraswat, "Optimization of intermetal dielectric deposition module using simulation," *J. Vac. Sci.*

Technol. B, vol. 13, no. 4, pp. 1867–1874, July/Aug. 1995.

[33] K. Maeda and S. M. Fisher, "CVD TEOS/O_3: Development history and applications," *Solid State Technol.*, pp. 83–88, June 1993.

[34] H. J. Oh, S. W. Rhee, and I. S. Kang, "Simulation of CVD process by boundary integral technique," *J. Electrochem. Soc.*, vol. 139, no. 6, pp. 1714–1720, June 1992.

[35] Watkins-Johnson Company, APCVD Process for SiO_2 and BPSG, 1995.

[36] S. Hamaguchi and S. M. Rossnagel, "Simulations of trench-filling profiles under ionized magnetron sputter metal deposition," *J. Vac. Sci. Technol. B*, vol. 13, no. 2, pp. 183–191, Mar./Apr. 1995.

[37] B. Haselden, P. Peavey, and B. Elicson, "Profile control and stringer removal during plasma etch of submicron meter polysilicon lines," in *SPIE Dry Proc. Submicron Litho.*, 1989, vol. 1185, pp. 115–127.

Ze-Kai Hsiau received the B.S. degree in electrical engineering from National Taiwan University, Taiwan, R.O.C, in 1988, in the top 5% of the class. He is currently a Ph.D. candidate in computer science at Stanford University, Stanford, CA. From 1988 to 1990, he served as a Second Lieutenant in the Marine Corps and maintained logistic databases on IBM and HP mainframes. He has been Numerical Analysis Consultant at Stanford Linear Accelerator Center and has held a summer position at Schlumberger Austin Research. His research interests include the boundary movement problem, VLSI fabrication process modeling, matrix computation, geometric algorithms, and computer graphics/visualization.

Edwin C. Kan (S'86–M'91) was born in Kaohsiung, Taiwan, R.O.C. in 1962. He received the B.S. degree from National Taiwan University, Taipei, in 1984, and the M.S. and Ph.D. degrees from the University of Illinois at Urbana-Champaign in 1988 and 1991, respectively, all in electrical engineering.

From 1984 to 1986, he served as a Second Lieutenant in the Air Force in Taiwan. In 1992, he joined Dawn Technologies as a Senior CAD Engineer developing advanced electronic and optical device simulators and technology CAD framework. He joined Stanford University, Stanford, CA, as a Research Associate in October 1993. His main research areas include the technology CAD development, semiconductor physics, and numerical methods.

James P. McVittie (M'75–SM'91) received the B.S.E.E. degree from the University of Illinois at Urbana-Champaign in 1967 and the M.S.E.E. and Ph.D. degrees from Stanford University, Stanford, CA, in 1968 and 1972, respectively.

From 1972 to 1974, he was a Technical Staff Member at MIT Lincoln Laboratory, where he worked on IV–VI materials for lasers and detectors. In 1974, he joined the Xerox Palo Alto Research Center where he worked on MOS interfaces and CCD's. He became a permanent member of Stanford's Integrated Circuit Laboratory Research Staff in 1981, where he worked on CMOS process development. Since 1985, he has headed a research group responsible for process development and modeling in CVD and plasma etch processes. His present research interests include plasma etching, CVD, metallization, oxidation, and semiconductor devices. He has coauthored more than 150 technical papers.

Dr. McVittie was a chairman of the Northern California Chapter of the American Vacuum Society in 1991. He was also chairman of the Bay Area Plasma Etch User's Group from 1989 to 1990, and the Northern California Electronic Materials Symposium in 1987. He is a past member of the Device Technology Committee for the International Electron Device Meeting (IEDM). He was the 1996 recipient of the Tegal Thinker Award for outstanding work in the area of plasma etching.

Robert W. Dutton (S'67–M'70–SM'80–F'84) received the B.S., M.S., and Ph.D. degrees from the University of California, Berkeley, in 1966, 1967, and 1970, respectively.

He has held summer staff positions at Fairchild, Bell Telephone Laboratories, Hewlett-Packard, IBM Research, and Matsushita during 1967, 1973, 1975, 1977, and 1988, respectively. Currently, he is Professor of Electrical Engineering at Stanford University, Stanford, CA, and Director of Research in the Center for Integrated Systems. His research interests focus on integrated circuit process, device, and circuit technologies—especially the use of computer-aided design and parallel computational methods.

Dr. Dutton has published more than 200 journal articles and graduated more than four dozen doctorate students. He was Editor of the IEEE TRANSACTIONS ON COMPUTER-AIDED DESIGN OF INTEGRATED CIRCUITS AND SYSTEMS from 1984 to 1986 and the winner of the 1987 IEEE J. J. Ebers and 1996 Jack Morton Awards. He received the 1988 Guggenheim Fellowship to study in Japan and was elected to the National Academy of Engineering in 1991.